

# Linking DC transport properties and entanglement negativity in non-Hermitian superlattices

L. S. Lima\*

Department of Physics, Federal Center for Technological Education of Minas Gerais,  
30510-000, Belo Horizonte, MG, Brazil. E-mail: lslima@cefetmg.br

(Dated: May 7, 2026)

## Abstract

We investigate how non-Hermitian effects in one-dimensional superlattices incorporating gain and loss imbalance, asymmetric hopping, and complex potentials modify both electrical transport and quantum correlations. Using a family of generalized Su–Schrieffer–Heeger (SSH) superlattice Hamiltonians with tunable sublattice asymmetry and non-reciprocity, we compute, linear response transport coefficients, and mixed-state entanglement measures across parameter regimes (*PT-symmetric broken regime*). We find robust signatures linking the onset of the skin effect and spectral winding to enhanced local currents and strongly inhomogeneous entanglement profiles, and topological edge modes to finite entanglement negativity in otherwise mixed steady states. Our results clarify when transport and entanglement provide complementary probes of non-Hermitian phase structure, and suggest experimental observables in photonic and cold-atom realizations.

## I. INTRODUCTION

In the past decade, non-Hermitian quantum systems have attracted growing attention as fertile grounds for realizing unconventional topological phases and transport phenomena that have no direct counterparts in Hermitian settings [1–18]. In contrast to Hermitian Hamiltonians, whose spectra are strictly real and whose topological properties are well captured by conventional

bulk–boundary correspondence, non-Hermitian systems generally exhibit complex energy spectra and host distinctive effects such as the non-Hermitian skin effect (NHSE) [19–22]. In the presence of open boundary conditions (OBC), the NHSE leads to an extensive accumulation of eigenstates near the system boundaries, profoundly modifying both spectral and transport properties. These features call for a reexamination of the foundations of topology and transport in quantum matter.

A paradigmatic model in the study of topological phases is the Su–Schrieffer–Heeger (SSH) model, which describes a one-dimensional dimerized lattice supporting topologically protected edge states [23]. Generalizations of the SSH model to higher dimensions, such as two-dimensional arrays of coupled SSH chains, provide a versatile framework for exploring richer band structures, including Dirac-like dispersions and higher-order topological phases [24, 25]. When nonreciprocal hopping processes and on-site gain and loss are introduced, these systems naturally enter the non-Hermitian regime, giving rise to novel spectral and topological characteristics that strongly influence their dynamical and transport behavior [26–28].

A key issue in this context is the role played by critical points associated with the closing and reopening of complex energy gaps, particularly under OBC, and how these spectral transitions manifest in experimentally accessible transport quantities such as electrical conductivity. While in Hermitian systems bulk gap closings typically coincide with topological phase transitions and leave clear signatures in transport, non-Hermitian systems often display boundary-sensitive spectral features that are absent under periodic boundary conditions (PBC), reflecting the breakdown of conventional bulk–boundary correspondence [20, 29, 30, 32].

In this work, we study electrical transport in non-Hermitian superlattices using the Kubo–Greenwood formalism. We analyze three gain–loss configurations (Fig. 1) with distinct impacts on multigap topology.

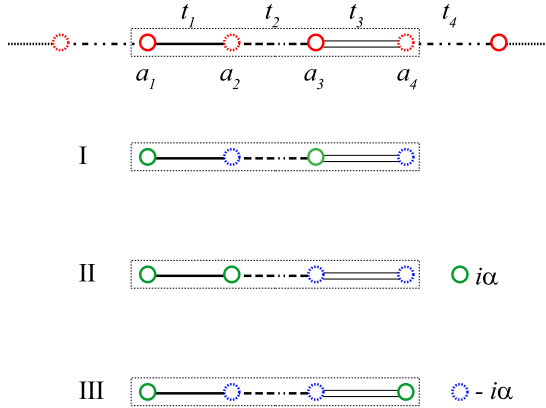


FIG. 1. Schematic representation of tetramerized superlattice with four sites (labeled by  $(a_1, a_2, a_3, a_4)$  per unit cell.  $t_1, t_2$  and  $t_3$  are the intracell couplings, whereas  $t_4$  is the intercell hopping. There are three different choices of balanced onsite gain and loss: case I with  $(i\alpha, -i\alpha, i\alpha, -i\alpha)$ , case II with  $(i\alpha, i\alpha, -i\alpha, -i\alpha)$ , and case III with  $(i\alpha, -i\alpha, -i\alpha, i\alpha)$ . The solid-green circles (dashed-blue circles) indicate positive (negative) imaginary parts,  $\pm\alpha$ .

For the  $\mathcal{PT}$ -symmetric pattern  $(i\alpha, -i\alpha, i\alpha, -i\alpha)$ , the multigap phases remain robust. In contrast, the configuration  $(i\alpha, i\alpha, -i\alpha, -i\alpha)$  suppresses the midgap topological phase. For the anti- $\mathcal{PT}$ -symmetric case  $(i\alpha, -i\alpha, -i\alpha, i\alpha)$ , a topological transition emerges in the midgap from trivial to nontrivial. The role of such gain-loss profiles on edge states was discussed in Ref. [31]. We further show that non-Hermitian parameters  $\alpha$ , incorporating nonreciprocity and gain-loss strength, strongly reshape both AC and DC conductivities [32–35]. Finally, we relate the entanglement negativity  $E_N$  to the Drude weight  $D_S$ , linking quantum correlations to coherent DC transport in non-Hermitian systems.

The remainder of this paper is organized as follows. In Section II, we introduce the model and analyzed the different phases, spectrum properties and topological edge states. In Section III, we compute the transport coefficients and quantifier of entanglement quantum correlation, analysing the interplay between DC conductivity and entanglement negativity. Finally, in Section IV, we discuss the physical implications of our findings and outline directions for future work.

## II. MODEL AND FORMALISM

The real-space Hamiltonian is given by

$$\begin{aligned} \mathcal{H} = & \sum_{j=1}^N \sum_{l=1}^3 \left[ t_n a_{j,l}^\dagger a_{j,l+1} + t_4 a_{j,4}^\dagger a_{j+1,1} + \text{H.c.} \right] \\ & + i\alpha \sum_{j=1}^N \left[ \sum_{l=1}^4 (-1)^{l+1} a_{j,1}^\dagger a_{j,1} + \sum_{l=1}^2 (a_{j,l}^\dagger a_{j,l}) - \sum_{l=3}^4 (a_{j,l}^\dagger a_{j,l}) \right] \\ & - i\alpha \sum_{j=1}^N \left[ \sum_{l=1}^2 (-1)^{l+1} a_{j,l}^\dagger a_{j,l} - \sum_{l=3}^4 (-1)^{l+1} a_{j,l}^\dagger a_{j,l} \right], \end{aligned} \quad (1)$$

with  $\alpha$  representing the gain or loss rate and  $t = t_1^2 + t_2^2 + t_3^2 + t_4^2$ . In the Hermitian limit, performing the Fourier transformation, the Block Hamiltonian is obtained as

$$\mathcal{H}_1(k) = t_1 \sigma_x \otimes \sigma^+ + t_2 \sigma_0 \otimes \sigma_0 + (t_4 e^{ik} - t_2) \sigma_0 \otimes \sigma_- + (t_4 e^{-ik} - t_2) \sigma_0 \otimes \sigma_+ + t_3 \sigma_x \otimes \sigma^- + i\alpha \sigma_0 \otimes \sigma_z \quad (2)$$

$$\mathcal{H}_2(k) = t_1 \sigma_x \otimes \sigma^+ + t_2 \sigma_0 \otimes \sigma_0 + (t_4 e^{ik} - t_2) \sigma_0 \otimes \sigma_- + (t_4 e^{-ik} - t_2) \sigma_0 \otimes \sigma_+ + t_3 \sigma_x \otimes \sigma^- + i\alpha \sigma_z \otimes \sigma_0 \quad (3)$$

where

$$\begin{aligned} \sigma_+ &= \begin{pmatrix} 0 & 1 \\ 0 & 0 \end{pmatrix}, & \sigma_- &= \begin{pmatrix} 0 & 0 \\ 1 & 0 \end{pmatrix} \\ \sigma^+ &= \begin{pmatrix} 1 & 0 \\ 0 & 0 \end{pmatrix}, & \sigma^- &= \begin{pmatrix} 0 & 0 \\ 0 & 1 \end{pmatrix}. \end{aligned}$$

The presence of non-Hermitian terms generates symmetries such as time-reversal  $\mathcal{T}_+ \mathcal{H}_{1,2}(k) \mathcal{T}_+^{-1} = \mathcal{H}_{1,2}(-k)$ , with  $\mathcal{T}_+ = \sigma_0 \otimes \sigma_0$ , particle-hole symmetry

$\eta \mathcal{H}_{1,2}^*(k) \eta^{-1} = -\mathcal{H}_{1,2}(-k)$  with  $\eta = \sigma_0 \otimes \sigma_z$ . Moreover, for  $t_1 = t_3$ ,  $\mathcal{H}_{1,2}(k)$  presents parity-time symmetry  $(\mathcal{PT}) \mathcal{H}_{1,2}(k) (\mathcal{PT})^{-1} = \mathcal{H}_{1,2}(k)$ , with  $\mathcal{P} = \sigma_x \otimes \sigma_x$ . In the following, we have that the multigap topological edge states of the superlattice exhibit distinct responses under different gain-loss patterns. Hereafter we set  $t_1 = t_3 = 1$  as the energy unit for simplicity.

### A. Phase diagram, spectral properties and topological edge states

The eigenvalues of Hamiltonian  $\mathcal{H}_1$  are given by

$$E_{\pm, \pm}(k) = \pm \sqrt{t/2 - \alpha^2 \pm (1/2) \sqrt{t^2 - 4F(k)}}, \quad (4)$$

where  $F(k) = t_1^2 t_3^2 + t_2^2 t_4^2 - 2t_1 t_2 t_3 t_4 \cos k$ . The band gaps between  $j$ th and  $(j+1)$ th bands are given at  $k = 0$  and  $k = \pi$  respectively. As  $\alpha$  is increased, five distinct regions can be defined: a  $\mathcal{PT}$ -symmetric phase for  $\alpha < \sqrt{t/2 - \sqrt{t^2/4 - F(0)}}$  where all eigenvalues are real. a  $\mathcal{PT}$ -broken phase when  $\sqrt{t/2 - \sqrt{t^2/4 - F(0)}} < \alpha < \sqrt{t/2 - \sqrt{t^2/4 - F(\pi)}}$ , which the central two bands have real and imaginary eigenvalues separated by exceptional points. A partial- $\mathcal{APT}$ -symmetric phase for  $\sqrt{t/2 - \sqrt{t^2/4 - F(\pi)}} < \alpha < \sqrt{t/2 + \sqrt{t^2/4 - F(\pi)}}$  where the eigenvalues are real for two bands and imaginary for other bands.  $\mathcal{PT}$ -broken phase when  $\sqrt{t/2 + \sqrt{t^2/4 - F(\pi)}} < \alpha < \sqrt{t/2 + \sqrt{t^2/4 - F(0)}}$ , of which two bands have real and imaginary eigenvalues separated by exceptional points.  $\mathcal{APT}$ -symmetric phase for  $\alpha > \sqrt{t/2 + \sqrt{t^2/4 - F(0)}}$  where the eigenvalues are purely imaginary.

In the Eq. (4), when  $t_1 = t_3$ ,  $t_2 = t_4$ , the first and third gaps close, while the second gap closes for  $t_1 t_3 = t_2 t_4$ , where at these gaps close signify the presence of topological phase transitions. Moreover, the topological properties can be characterized by the sum of Zak phases of all the isolated bands below the corresponding gap: topological phase of the first and third band gap with Zak phases  $\mathcal{Z}_1 = \pi, \mathcal{Z}_2 = 0$ . Region II represents the trivial phase with  $\mathcal{Z}_{1,2} = 0$ ; region III is the topological phase of the middle band gap  $\mathcal{Z}_1 = 0, \mathcal{Z}_2 = \pi$ ; region IV is the completely topological phase with  $\mathcal{Z}_{1,2} = \pi$ . The boundaries coincide with the locations of gap-closing points. The nontrivial Zak phase implies that a pair of topologically protected edge states will emerge at the boundaries of the finite lattice according to bulk-edge correspondence.

$$\begin{aligned} \mathcal{Z}_l &= i \int_{-\pi}^{\pi} (\langle \psi_1(k) | \partial_k | \psi_1(k) \rangle + \langle \psi_2(k) | \partial_k | \psi_2(k) \rangle \\ &\quad + \dots + \langle \psi_l(k) | \partial_k | \psi_l(k) \rangle) dk \mod 2\pi, \end{aligned}$$

where  $|\psi_l(k)\rangle$  is the Bloch wave functions with eigenvalue  $E_l$ . Furthermore, the Zak phase can take only the values

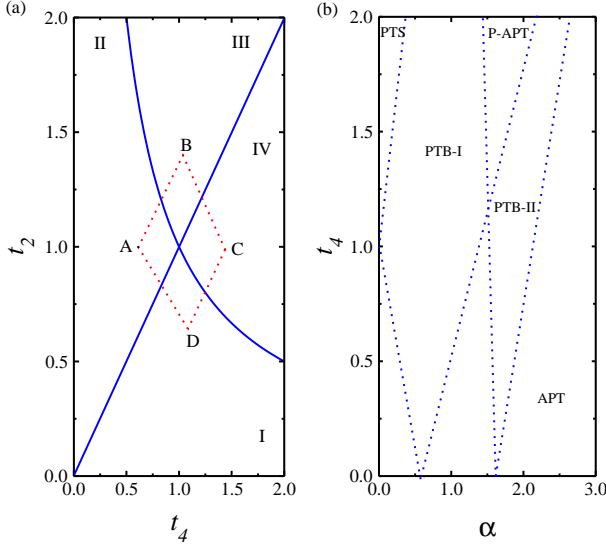


FIG. 2. Plot (a) Phase diagram of the Hermitian topological superlattice: region I is the topological phase of the first and third band gap with Zak phases  $\mathcal{Z}_1 = \pi, \mathcal{Z}_2 = 0$ ; region II represents the trivial phase with  $\mathcal{Z}_{1,2} = 0$ ; region III is the topological phase of the middle band gap  $\mathcal{Z}_1 = 0, \mathcal{Z}_2 = \pi$ ; region IV is the completely topological phase with  $\mathcal{Z}_{1,2} = \pi$ . Plot (b) Phase diagram of the non-Hermitian Hamiltonian  $\mathcal{H}_1$  with  $t_2 = 1$ , which contains a  $\mathcal{PT}$ -symmetric (PTS) phase where all eigenvalues are real, two  $\mathcal{PT}$ -broken (PTB I and PTB II) phases with real and imaginary eigenvalues separated by exceptional points, a partial  $\mathcal{APT}$ -symmetric (APT) phase with purely imaginary energies.

zero or  $\pi$ , denoting the trivial and nontrivial topological phases, respectively.

In Fig. 2 (a), we show the phase diagram  $t_4$  vs  $t_2$  of the Hermitian topological superlattice ( $\alpha = 0$ ). The four distinct phases are represented: region I which is the topological phase of the first and third band gap with Zak phases  $\mathcal{Z}_1 = \pi, \mathcal{Z}_2 = 0$ . Region II which represents the trivial phase with  $\mathcal{Z}_{1,2} = 0$ ; region III which is the topological phase of the middle band gap  $\mathcal{Z}_1 = 0, \mathcal{Z}_2 = \pi$ ; region IV which is the completely topological phase with  $\mathcal{Z}_{1,2} = \pi$ .

In Fig. 2 (b), we present the phase diagram of the non-Hermitian  $\mathcal{H}_1$  with  $t_2 = 1$ . The phase diagram contains five distinct phases:  $\mathcal{PT}$ -symmetric (PTS) phase where all eigenvalues are real, two  $\mathcal{PT}$ -broken (PTB I and PTB II) phases with real and imaginary eigenvalues separated by exceptional points, a partial  $\mathcal{APT}$ -symmetric (APT) phase with purely imaginary energies.

For the non-Hermitian superlattice governed by the Hamiltonian  $\mathcal{H}_2(k)$ , its eigenvalues for  $t_1 = t_3$  are given by

$$E_{\pm,\pm}(k) = \pm \sqrt{(t - 2\alpha^2) \pm (1/2)\sqrt{G(k) - 16\alpha^2 t_1^2}}, \quad (5)$$

where  $G(k) = (t_2^2 - t_4^2)^2 + 4t_1^2 t_2^2 + 4t_1^2 t_4^2 + 8t_1^2 t_2 t_4 \cos k$ .

Supposing the midgap  $\Delta E = 0$ , we have

$$\alpha_c^\pm = \sqrt{\pm(1/2) \left[ \sqrt{G(0) - t^2 + (2t_1^2 - t_2^2 - t_4^2)^2} - t_1^2 + t_2^2/2 + t_4^2/2 \right]},$$

where the mid-gap is gapless when  $\alpha_c^- < \alpha < \alpha_c^+$ .

For small values of  $\alpha$ , the energy bands remain entirely real and gapped, indicating that  $\mathcal{PT}$  symmetry is preserved. As the degree of non-Hermiticity increases, the upper and lower bands approach and eventually touch their adjacent bands, accompanied by the exceptional points. In this regime,  $\mathcal{PT}$  symmetry is broken for the top and bottom bands, while it remains intact within the intermediate gaps. Concurrently, the gap between the two bands gradually closes. With a further increase in the gain-loss rate  $\alpha$ ,  $\mathcal{PT}$  symmetry becomes spontaneously broken for the middle bands as well. Interestingly, upon increasing  $\alpha$  beyond this regime, the middle bands recover real-valued spectra, and the corresponding midgap reopens with an enlarged separation.

## B. Topological Invariants

The one-dimensional non-Hermitian chiral-symmetric system:  $\Gamma \mathcal{H}'(k) \Gamma^{-1} = -\mathcal{H}'(k)$  has its topological properties characterized by Chern number [36]. The Chern number is obtained for a 2D effective Hermitian Hamiltonian  $\mathcal{H}_e(k, \varepsilon) = \Gamma[\varepsilon - i\mathcal{H}(k)]$ , with  $\Gamma = \sigma_0 \otimes \sigma_z$  and  $\varepsilon$  denotes the imaginary part of the energy. To overcome the periodicity of  $\varepsilon$ , we define  $\mathcal{H}'_e(k, \varepsilon) = \mathcal{R}_\delta \mathcal{H}_e(k, \varepsilon) \mathcal{R}_\varepsilon^\dagger$  with  $\mathcal{R}_\varepsilon = \exp[i\frac{\pi}{4}(1 + \tanh \varepsilon)\mathcal{G}]$ , where  $\mathcal{G} = \sigma_x \otimes \sigma_0$ . Thus, the Chern number is obtained as

$$C = \lim_{\varepsilon \rightarrow \infty} \frac{\varepsilon}{2\pi} \int_{-\pi}^{\pi} \Omega(k) dk, \quad (6)$$

where

$$\lim_{\varepsilon \rightarrow \infty} \mathcal{H}'_e(k, \varepsilon) = \lim_{\varepsilon \rightarrow -\infty} \mathcal{H}'_e(k, \varepsilon) = |\varepsilon| \Gamma$$

due to  $\mathcal{R}_{-\infty} = \sigma_0 \otimes \sigma_0$ ,  $\mathcal{R}_{-\infty} = i\mathcal{G}$  and

$$\Omega(k) = \sum_{n \leq n_F, m > n_F} \text{Im} \left\{ 2 \langle \psi^{nm}(k) | \mathcal{H}'_e(k) | \psi^{mn}(k) \rangle \times \frac{\langle \psi^{mn}(k) | \mathcal{H}'_e(k) | \psi^{nm}(k) \rangle}{(E_{nm}(k) - E_{mn}(k))^2} \right\}, \quad (7)$$

where  $n_F$  is the number of occupied bands,  $|\psi^{mn}(k)\rangle$  is eigenstate of  $\mathcal{H}'(k)$  with eigenvalues  $E_{mn}(k)$ . The Chern number  $C$  is an integer, and its value remains strictly constant under smooth perturbations that preserve the band gap separating the occupied and empty bands.

## III. RESULTS AND DISCUSSION

### A. Transport coefficients

We get the current operator continuity Equation  $\mathcal{J}$  from  $\partial \rho / \partial t + \nabla \cdot \mathcal{J} = \mathcal{J}_N^{1,2}$  where  $\rho = a^\dagger(\mathbf{x}, t) a(\mathbf{x}, t)$  and

$\mathcal{J}_N^{1,2}$  is the contribution of the dissipative non-Hermitian term. We found

$$\mathcal{J}_{il} = 2i \sum_{j=1}^N \sum_{l=1}^3 [t_n(a_{j,l}^\dagger a_{j,l+1} - a_{j,l+1}^\dagger a_{j,l}) + t_4(a_{j,l}^\dagger a_{j+1,l} - a_{j+1,l}^\dagger a_{j,l})] + \mathcal{J}_N^{1,2} \quad (8)$$

The longitudinal electric conductivity at  $q = 0$  in  $x$  direction is given by [37]

$$\sigma(\omega) = -\frac{i}{N} \sum_{m,n=\pm} \sum_k \left[ \frac{p_{nm}(k) - p_{mn}(k)}{E_{nm}(k) - E_{mn}(k)} \right] \times \frac{\langle k, nm | \mathcal{J}(k) | k, mn \rangle \langle k, m | \mathcal{J}(k) | k, nm \rangle}{E_{nm}(k) - E_{mn}(k) + \omega + i0^+}, \quad (9)$$

where  $E_{nm}(k)$   $n, m = \pm$  are the energies of the  $n, m$ th bands and  $p(x) = (e^x + 1)^{-1}$ , with  $x = E_{nm}(k)/k_B T$  is the Fermi-Dirac distribution function.  $\mathcal{J}(k)$ , is the electric current operator, at point  $k$  into the first Brillouin zone given by [38]. From above formula, we get the real part of the dynamical conductivity given by [39, 40]:

$$\text{Re}\sigma(\omega) = D_S(T)\delta(\omega) + \sigma^{reg}(\omega), \quad (10)$$

where

$$D_S(T) = \frac{\pi}{N} \sum_{n,m=\pm} \sum_k \frac{\partial p_{nm}(k)}{\partial E_{nm}(k)} \langle k, nm | \mathcal{J}(k) | k, nm \rangle \langle k, nm | \mathcal{J}(k) | k, nm \rangle, \\ \sigma^{reg}(\omega) = -\frac{1}{N} \sum_{n,m=\pm} \sum_k \left[ \frac{p_{nm}(k) - p_{mn}(k)}{E_{nm}(k) - E_{mn}(k)} \right] \times \langle k, nm | \mathcal{J}(k) | k, mn \rangle \langle k, mn | \mathcal{J}(k) | k, n \rangle \delta(\omega - E_{nm}(k) - E_{mn}(k)), \quad (11)$$

where

$$D_S(T) = \frac{\pi}{N} \sum_{n,m=\pm} \sum_k \left\{ (t_1 + t_2 + t_3 - t_4)^2 \sin(k) \times \tanh\left(\frac{E_{nm}(k) - E_{mn}(k)}{2k_B T}\right) - (t_1 + t_2 + t_3 - t_4)^2 \cos^2(k) \left[ \frac{p_{nm}(k) - p_{mn}(k)}{E_{nm}(k) - E_{mn}(k)} \right] \right. \\ \times \left[ 1 - e^{(E_{nm}(k) - E_{mn}(k))/k_B T} \right] \mathcal{P}\left(\frac{1}{E_{nm}(k) - E_{mn}(k) + \omega}\right), \\ \sigma^{reg}(\omega) = \sum_{n,m=\pm} \sum_k (t_1 + t_2 + t_3 - t_4)^2 \cos^2(k) \times \left[ \frac{p_{nm}(k) - p_{mn}(k)}{E_{nm}(k) - E_{mn}(k)} \right] \left[ 1 - e^{(E_{nm}(k) - E_{mn}(k))/k_B T} \right] \\ \times \delta(E_{nm}(k) - E_{mn}(k) + \omega) \quad (12)$$

where  $\mathcal{P}(\dots)$  means principal value.

The Kubo formula is extended to non-Hermitian systems, with the conductivity  $\sigma(\omega)$  depending on the current operator  $\mathcal{J}(k)$  with the modifications made to account for the complex energy spectrum and biorthogonal basis, and provide a validation against the known

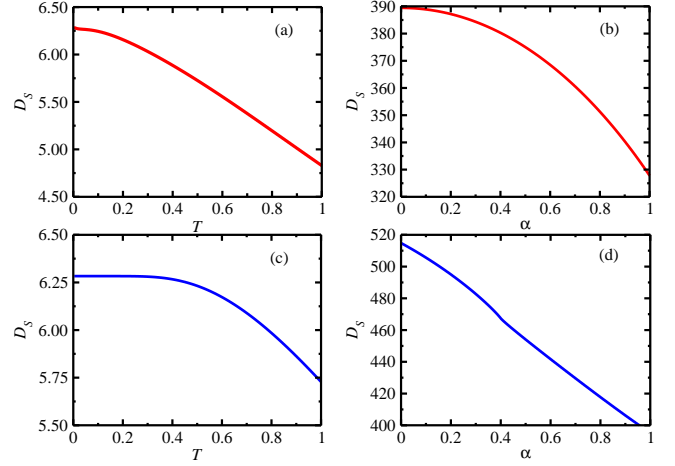


FIG. 3. Plots (a) and (b)  $D_S$  vs.  $T$  for  $\alpha = 0.5$  and  $D_S$  vs.  $\alpha$  for  $T = 0.01$  for the Hamiltonian  $\mathcal{H}_1$ . Plots (c) and (d)  $D_S$  vs.  $T$  for  $\alpha = 0.5$  and  $D_S$  vs.  $\alpha$  for  $T = 0.01$  for the Hamiltonian  $\mathcal{H}_2$ .

Hermitian case to ensure accuracy. The differences are: Biorthogonal matrix elements, where both numerators involve left-right matrix elements; no complex conjugation appears by default. The Complex poles, where denominators carry complex transition energies; their imaginary parts regularize the  $\omega \rightarrow 0$  behavior and encode gain/loss-induced broadening. The causality, where the retarded prescription  $+i0^+$  is kept, ensuring the same analyticity and Kramers-Kronig structure for the retarded correlator and stability required.

The key reasons the Kubo formula survives in many non-Hermitian settings are as following: In first, if the non-Hermitian Hamiltonian  $\mathcal{H}_{\text{eff}}$  is used to describe the system, and a pseudo-equilibrium or steady state is reached via coupling to a reservoir, the system may still exhibit equilibrium-like features. The steady state can resemble a thermal Gibbs-like state in a biorthogonal ensemble. Moreover, in open quantum systems, fluctuation and response functions can be defined using Keldysh field theory. Even in the presence of non-Hermiticity, Kubo-type linear response functions can be formulated, and the fluctuation-dissipation relation can be preserved if the dynamics equilibrate and satisfy stationarity and causality in the effective description. In some non-Hermitian systems, effective unitarity can emerge in the unbroken-symmetric phase, allowing fluctuation-dissipation relation to hold within certain parameter regimes [7, 9].

In Fig. 3, we show the Drude weight  $D_S(T)$  as a function of temperature  $T$  and non-Hermiticity  $\alpha$ . In the limit  $T \rightarrow 0$ ,  $D_S$  remains finite, implying a divergent DC conductivity. At finite temperature or in the presence of disorder, the delta peak  $\delta(\omega)$  in  $\text{Re}\sigma(\omega)$  broadens into a Lorentzian, yielding a finite conductivity. Following Ref. [42], the Drude weight is defined as  $D_S(T) = \langle K \rangle - \Lambda(k=0, \omega)$ , where  $\langle -K \rangle$  is the kinetic energy and  $\Lambda(k, \omega)$  the current-current correlation

function. In the limit  $\omega \rightarrow 0$ ,  $\text{Re}\sigma(\omega)$  contains a singular term  $D_S\delta(\omega)$ , signaling dissipationless transport. The Meissner response instead probes the static ( $\omega = 0$ ) transverse limit. For  $k \rightarrow 0$ , the superfluid stiffness is  $D = \pi[-K] - \Lambda(k \rightarrow 0, i\omega_n = 0)$ , with  $i\omega_n = \omega + i0^+$ . The distinction between  $D_S$  and  $D$  arises from the non-commutativity of the limits  $k \rightarrow 0$  and  $\omega \rightarrow 0$ . Physically,  $D_S$  measures the charge stiffness, while  $D$  quantifies the superfluid density. In the thermodynamic limit at  $T = 0$  and without disorder, these quantities characterize the ground state:  $D_S, D \neq 0$  for a superconductor;  $D_S \neq 0, D = 0$  for a metal; and  $D_S = D = 0$  for an insulator.

## B. Quantum correlations and entanglement

Entanglement negativity  $E_N$  is defined as the logarithm of the trace norm of the partial transpose of the density matrix of the system  $\rho_A$ . Overall, the entanglement negativity is a powerful tool for characterizing the entanglement properties of quantum systems, and its behavior can provide important insights into the fundamental properties of quantum mechanics and potential applications of quantum information science. However,  $E_N$  presents a large deficiency i.e. a failure in satisfying the discriminant property, either that the entanglement  $E_N(\rho) = 0$  if and only if  $\rho$  is separable [41]. It is used much often as a measure of thermal entanglement for disjoint intervals.  $E_N$  is given for a mixed state  $\rho_{GE}$  by [43, 44]

$$N(\rho) = \frac{\|\rho_A^T\|_1 - 1}{2}, \quad (13)$$

where  $\|X\|_1 = \text{Tr}|X| = \text{Tr}\sqrt{X^\dagger X}$  is the trace norm and  $\rho_A^T$  is the partial transpose of  $\rho_A$  with respect to the subsystem  $A$ . The logarithmic negativity is [43]

$$E_N(\rho) = \log_2 \|\rho_A^T\|_1. \quad (14)$$

In general, the system will thermalise when the Gibbs distribution  $\rho$ , is given by  $\rho \propto e^{-\mathcal{H}/k_B T}$ , where the statistical ensemble describing the system for long time is expected to be the canonical ensemble, being the density matrix of the canonical ensemble given by [45–47].

The quantum state evolves in time under the non-Hermitian Hamiltonian  $\mathcal{H}(t)$  as the model Eq. (1), according to the von Neumann equation

$$i\hbar \frac{\partial \rho(t)}{\partial t} = [\mathcal{H}(0), \rho] + \{\mathcal{H}_1(t), \rho\} \quad (15)$$

where  $\rho(0) = \rho_0$ ,  $\mathcal{H}_1(t) = -if(t)A(t)$ , with  $A(t) = e^{i\mathcal{H}_0 t/\hbar} A e^{-i\mathcal{H}_0 t/\hbar}$ .  $f(t)$  is a non-negative time-dependent function for instance, a rectangular pulse of strength  $s$  and duration  $\delta t$ ,  $f(t) = \hbar s [\theta(t - t_w) - \theta(t - t_w - \delta t)]/\delta t$  ( $\theta(x)$  is the step function) at fixed waiting time  $t_w$ . To linear order in the perturbation theory, we can write

$$\rho(t) = \rho_0 - \hbar^{-1} \int_0^t dt' \{\mathcal{H}_1(t'), \rho_0\} f(t') \quad (16)$$

where one gets

$$\text{Tr}[\rho(t)] = 1 - 2\hbar^{-1} \int_0^t dt' \langle 0|A(t')|0\rangle f(t'). \quad (17)$$

We say that the system relaxes locally if the limit  $\lim_{t \rightarrow \infty} \lim_{N \rightarrow \infty} \rho_A(t) = \rho_A(\infty)$  exists for any finite subsystem  $A$ . Its stationary state is defined as  $\lim_{N \rightarrow \infty} \text{Tr}_B(\rho) = \rho_A(\infty)$ , where  $B$  is the complement of  $A$ . In the absence of other conserved quantities isolated systems thermalize to thermal equilibrium

$$\rho = \rho^{Gibbs} = [\text{Tr}(e^{-\beta \mathcal{H}})]^{-1} e^{-\beta \mathcal{H}},$$

where  $\beta$  is fixed by the initial value of the energy density

$$h \equiv \lim_{N \rightarrow \infty} \frac{1}{N} \text{Tr}(\rho^{Gibbs} \mathcal{H}).$$

Thus, we get  $\rho$  as

$$\rho = Z^{-1} e^{-\frac{1}{k_B T} \sum_{n=\pm, m=\pm} \sum_k E_{nm}(k) a_k^\dagger a_k},$$

where  $Z$  is the partition function. The entanglement negativity is given by

$$E_N = -\log_2 \left( Z^{-1} e^{-\frac{1}{k_B T} \sum_{n=\pm, m=\pm} \sum_k E_{nm}(k) p(E_{nm}(k))} \right). \quad (18)$$

We assume a thermal state associated with an effective Hamiltonian, for which the resulting density matrix is mathematically well defined and physically motivated through a connection to an effective equilibrium description. An alternative and more general approach for a non-Hermitian Hamiltonian such as Eq. (1) is to explicitly determine the steady-state density matrix by solving a Lindblad master equation, thereby modeling the coupling to the environment. In this framework, the steady state  $\rho_{ss}$  can be obtained either from the long-time limit of the non-unitary dynamics or within a biorthogonal formalism, allowing the entanglement negativity to be evaluated for a genuinely non-thermal state.

The bipartition of the system plays a crucial role in the interpretation of the entanglement negativity. A common choice is to divide the chain at symmetry-related locations or at regions of particular physical relevance, such as the center of the system, where topological edge or interface states may emerge in certain phases. Alternatively, one can systematically shift the cut along the chain and monitor the spatial dependence of  $E_N$ , which provides insight into how quantum correlations are distributed across the lattice.

More generally, the choice of bipartition is not merely a geometric consideration but a diagnostic tool tailored to the specific topological features under investigation. Depending on the location of the partition,  $E_N$  can probe distinct aspects of the underlying topological phase, including edge states, bulk entanglement patterns, and the influence of non-Hermitian effects. By judiciously selecting the bipartition, one can therefore access information about topological invariants and uncover how non-Hermiticity reshapes the entanglement structure in comparison to the Hermitian limit.

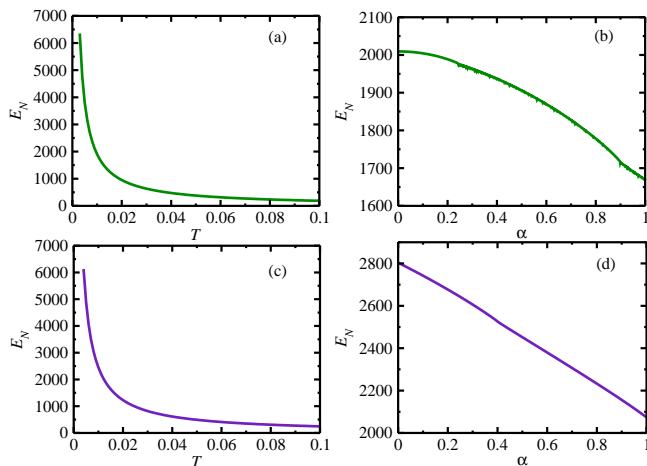


FIG. 4. Plots (a) and (b)  $E_N$  vs.  $T$  for  $\alpha = 0.5$  and  $E_N$  vs.  $\alpha$  for  $T = 0.01$  for the Hamiltonian  $\mathcal{H}_1$ . Plots (c) and (d)  $E_N$  vs.  $T$  for  $\alpha = 0.5$  and  $E_N$  vs.  $\alpha$  for  $T = 0.01$  for the Hamiltonian  $\mathcal{H}_2$ .

Typically, one might choose the bipartition of the chain at symmetry points or regions of interest, such as at the center of the chain, where topological edge states are expected to reside in certain phases. Alternatively, one might study how  $E_N$  changes as the cut is moved across different sites, which can provide insight into how entanglement is distributed throughout the system.

We analyzed quantum correlations via entanglement negativity in a subsystem of  $N$  spins block, considering the partition with  $N$  spins for which the local entropy is calculated and in following making  $N \rightarrow \infty$  in the partition, for the continuum theory is valid. Moreover, We assume a thermal state for a effective Hermitian Hamiltonian correspondent to the non-Hermitian model Eq. (1), the result thus is mathematically defined and physically justified by a connection to an effective equilibrium. However, an another approach for a non-Hermitian Hamiltonian as Eq. (1), is to compute the true steady-state density matrix from the Lindblad equation (if we model the open system environment explicitly), either from the long-time limit of non-unitary evolution or from a biorthogonal formalism, where we compute the entanglement negativity from the non-thermal  $\rho_{ss}$ .

In Fig. 4, we present the temperature dependence of the entanglement negativity  $E_N$ . As  $T \rightarrow 0$ ,  $E_N$  exhibits a pronounced divergence, which can be attributed to the strong enhancement of quantum fluctuations in the zero-temperature limit. In addition, we observe that increasing the non-Hermitian parameter leads to only minor quantitative changes in the  $E_N$  curves. This weak sensitivity reflects the fact that the overall symmetry of the energy spectrum undergoes an abrupt transition from being predominantly real to predominantly imaginary, without substantially altering the low-temperature scaling behavior of the entanglement.

## C. Discussion

*Observable signatures of spectral splitting:* When spectral splitting occurs along the real-energy axis, the system exhibits two distinct resonant frequencies, resulting in a characteristic double-peak structure in the transmission or optical response as a function of frequency. In contrast, splitting along the imaginary-energy axis leads to a single resonance, accompanied by asymmetric linewidths and pronounced variations in amplitude or effective gain. This behavior can be quantitatively identified through linewidth analysis or by examining growth-decay dynamics. Concomitantly, the corresponding eigenstate profiles undergo a qualitative transformation, evolving from spatially extended modes to boundary-localized states. Such edge localization can be directly probed via near-field imaging techniques in photonic platforms or through site-resolved occupation measurements in cold-atom systems. Importantly, the emergence of non-Bloch Dirac points is reflected in abrupt variations of the Drude weight, while discontinuities or sharp features in the regular conductivity provide clear signatures of these spectral transitions.

*Identification of conductivity resonances:* The position of non-Bloch Dirac points relative to the surrounding energy gaps plays a decisive role in determining the resonant frequencies associated with interband optical transitions. When a non-Bloch Dirac point is situated deep within a real line-gapped phase, the optical gap remains well defined, giving rise to sharp and well-resolved peaks in the optical conductivity. Conversely, as the Dirac point approaches the boundary of a complex-energy region, the effective gap narrows or closes, leading to significant broadening of the conductivity peaks due to the finite imaginary components of the eigenvalues. This regime is typically accompanied by an enhanced low-frequency response. Within this framework, the frequency window  $(\omega - \omega_0)$  serves as a direct probe of transitions relative to the lowest excitation threshold set by the non-Bloch gap. As the Dirac points move closer to the gap edges, the threshold frequency decreases, and the corresponding conductivity features become increasingly pronounced.

*Numerical assessment of robustness and signal-to-noise:* Although both  $D_S$  and  $\sigma^{reg}(\omega)$  are derived analytically, their robustness can be quantitatively validated through numerical simulations. To this end, we introduce weak random perturbations of small amplitude to the Hamiltonian matrix elements and repeat the transport calculations over a large ensemble of disorder realizations. The resulting noise level is quantified by the standard deviation of the corresponding observable. In addition, we examine the sensitivity of the results to the choice of the infinitesimal imaginary regulator ( $i0_+$ ) entering the response functions. Finally, by comparing results obtained using thermal occupation factors at low temperature with those based on step-function occupations, we assess the stability of  $D_S$  and  $\sigma^{reg}(\omega)$  with respect to both numer-



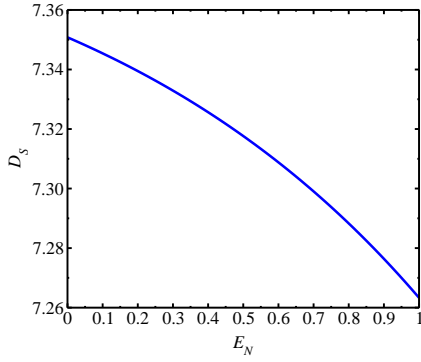


FIG. 5.  $D_S$  vs  $E_N$ , at low temperature:  $T = 0.01J$  held fixed.

ical and physical regularization schemes.

#### D. Linking $D_S$ and $E_N$

From Eqs. (12) and (18), we found the link between  $D_S$  and  $E_N$  in the following way

$$D_S(T) = \frac{\pi}{N} \sum_k (t_1 + t_2 + t_3 - t_4) \sin k \left( \frac{e^{E_N/2} - Ze^{-E_N/2}}{e^{E_N/2} + Ze^{-E_N/2}} \right) - (t_1 + t_2 + t_3 - t_4)^2 \left[ \frac{\cos^2(k)}{k_B T (\log_2 Z - E_N)} \right] \left[ 1 - \frac{Ze^{-E_N} - 1}{Z^{-1}e^{E_N} - 1} \right] \times \mathcal{P} \left( \frac{1}{k_B T (\log_2 Z - E_N) + \omega} \right), \quad (19)$$

In Fig. 5, we plot the Drude weight  $D_S$  vs.  $E_N$  as a way to clarify the relationship between entanglement negativity and DC conductivity. We found that the Drude weight of the electric conductivity remains finite even in

the limit where  $E_N \rightarrow 0$ , i.e., when quantum correlations are absent. As  $E_N$  increases, the Drude weight exhibits a slight decrease, demonstrating that there is slight dependence of the DC conductivity vs  $E_N$ . Physically, this behavior indicates that stronger quantum correlations tend to inhibit coherent charge transport, while regimes with reduced entanglement are more favorable to metallic conduction.

#### IV. SUMMARY AND OUTLOOK

We analyze the link between DC transport and quantum correlations given by entanglement negativity in one-dimensional superlattices.

The Skin effect further amplifies boundary disorder, making robust observation challenging. Moreover, measurement of transport are sensitive to complex-frequency conductivity e.g., THz spectroscopy in photonics, or AC impedance in topoelectrical circuits. Direct observation of sixth-order scaling in condensed matter physics is likely impractical. Synthetic platforms are more realistic.

From a broader perspective, studying the AC and DC conductivities of the SSH model is essential for understanding the low-temperature transport properties of topological insulators, especially when non-Hermitian effects are present. Our results highlight how non-Hermiticity fundamentally alters the transport response, revealing new routes to engineer and control electronic properties in low-dimensional topological systems.

**Corresponding author:**

\*E-mail: lslima@cefetmg.br.

**Funding Declaration:**

This research has received none funding.

**Data availability:**

All data generated or analysed during this study are included in this manuscript.

#### REFERENCES

- 
- [1] E. J. Bergholtz, J. Carl Budich, F. K. Kunst, Exceptional topology of non-Hermitian systems, *Rev. Mod. Phys.*, 93, 015005 (2021).
  - [2] Y. Ashida, Z. Gong, M. Ueda, Non-Hermitian physics, *Adv. Phys.* 69, 249 (2020).
  - [3] Z. Gong, Y. Ashida, K. Kawabata, K. Takasan, S. Higashikawa, M. Ueda, Topological Phases of Non-Hermitian Systems, *Phys. Rev. X*, 8, 031079 (2018).
  - [4] S. Yao, Z. Wang, Edge States and Topological Invariants of Non-Hermitian Systems, *Phys. Rev. Lett.* 121, 086803 (2018).
  - [5] C. Gardiner and P. Zoller, *Quantum Noise: A Handbook of Markovian and Non-Markovian Quantum Stochastic Methods with Applications to Quantum Optics*, 3rd ed., Springer Series in Synergetics, Springer-Verlag Berlin Heidelberg (2004).
  - [6] H.-P. Breuer and F. Petruccione, *The Theory of Open Quantum Systems*, Oxford University Press, Oxford (2007).
  - [7] L. Pan, X. Chen, Y. Chen, H. Zhai, Non-Hermitian linear response theory, *Nat. Phys.* 16, 767 (2020).
  - [8] A. Hashemi, K. Busch, D. N. Christodoulides, S. K. Ozdemir, R. El-Ganainy, Linear response theory of open systems with exceptional points, *Nat. Commun.* 13, 3281 (2022).
  - [9] Kevin T. Geier, Philipp Hauke, From Non-Hermitian Linear Response to Dynamical Correlations and Fluctuation-Dissipation Relations in Quantum Many-Body Systems, *Phys. Rev. X Quantum* 3, 030308 (2022).
  - [10] N. Moiseyev, *Non-Hermitian Quantum Mechanics*, Cambridge University Press, Cambridge, UK (2011).
  - [11] Correlations at  $\mathcal{PT}$ -Symmetric Quantum Critical Point, *Phys. Rev. Lett.* 128, 146804 (2022).
  - [12] L. Jin, Z. Song, Symmetry-Protected Scattering in Non-Hermitian Linear Systems, *Chin. Phys. Lett.* 38, 024202 (2021).

- [13] Yan-Gang Miao, Zhen-Ming Xu, Investigation of non-Hermitian Hamiltonians in the Heisenberg picture, *Phys. Lett. A* 380, 1805 (2016).
- [14] Leonardo S. Lima, Non-Hermitian linear-response theory for spin diffusion in quantum systems, *Sci. Rep.* 14, 17536 (2024).
- [15] L. S. Lima, Spin transport in non-Hermitian quantum systems, *Sci. Rep.* 13, 11112 (2023).
- [16] L. S. Lima, Linear response theory for transport in non-Hermitian  $\mathcal{PT}$ -symmetric models, *Phys. Lett. A* 525, 129923 (2024).
- [17] L. S. Lima, Transport in (4+1)-D-dimensional topological insulators models, *Phys. Lett. A* 384, 126514 (2020).
- [18] L. S. Lima, Transport in  $Z_2$  invariant in one and two-dimensional topological insulators models, *Physica E* 113, 208 (2019).
- [19] S. Yao, F. Song, Z. Wang, Non-Hermitian Chern Bands, *Phys. Rev. Lett.*, 121, 136802 (2018).
- [20] Flore K. Kunst, E. Edvardsson, Jan Carl Budich, Emil J. Bergholtz, Biorthogonal Bulk-Boundary Correspondence in Non-Hermitian Systems, *Phys. Rev. Lett.*, 121, 026808 (2018).
- [21] T. Helbig, T. Hofmann, S. Imhof, M. Abdelghany, T. Kiessling, L. W. Molenkamp, C. H. Lee, A. Szameit, M. Greiter & R. Thomale, Generalized bulk-boundary correspondence in non-Hermitian topoelectrical circuits, *Nature Phys.*, 16, 747–750 (2020).
- [22] S. Weidemann, M. Kremer, T. Helbig, T. Hofmann, A. Stegmaier, M. Greiter, R. Thomale, A. Szameit, Topological funneling of light, *Science*, 368, 311–314 (2020).
- [23] W. P. Su, J. R. Schrieffer, A. J. Heeger, Solitons in Polyacetylene, *Phys. Rev. Lett.* 42, 1698 (1979).
- [24] W. A. Benalcazar, B. A. Bernevig, T. L. Hughes, Quantized electric multipole insulators, *Science*, 357, 61–66 (2017).
- [25] Lin et al., *Phys. Rev. B*, 99, 235421 (2019).
- [26] Tony E. Lee, *Phys. Anomalous Edge State in a Non-Hermitian Lattice*, *Rev. Lett.*, 116, 133903 (2016).
- [27] Y. Xiong, Why does bulk boundary correspondence fail in some non-hermitian topological models, *J. Phys. Commun.*, 2, 035043 (2018).
- [28] S. Longhi, Topological Phase Transition in non-Hermitian Quasicrystals, *Phys. Rev. Lett.*, 122, 237601 (2019).
- [29] N. Okuma, K. Kawabata, K. Shiozaki, M. Sato, Topological Origin of Non-Hermitian Skin Effects, *Phys. Rev. Lett.*, 124, 086801 (2020).
- [30] K. Zhang, Z. Yang, C. Fang, Correspondence between Winding Numbers and Skin Modes in Non-Hermitian Systems, *Phys. Rev. Lett.*, 125, 126402 (2020).
- [31] G. Zhang, J. Kang, C. Wu, D. Zheng, Y. Zhou, W. Bao, G. Chen, Multigap topology engineering in non-Hermitian superlattice, *Phys. Rev. A* 112, 043549 (2025).
- [32] K. Kawabata, K. Shiozaki, M. Ueda, M. Sato, Symmetry and Topology in Non-Hermitian Physics, *Phys. Rev. X*, 9, 041015 (2019).
- [33] K. Yokomizo, S. Murakami, Non-Bloch Band Theory of Non-Hermitian Systems, *Phys. Rev. Lett.*, 123, 066404 (2019).
- [34] Zhang et al., *Phys. Rev. B*, 101, 041101 (2020).
- [35] Zhi-Qiang Zhang, Bing-Lan Wu, Juntao Song, Hua Jiang, Topological Anderson insulator in electric circuits, *Phys. Rev. B*, 100, 184202 (2019).
- [36] W. Brzezicki and T. Hyart, Hidden Chern number in one-dimensional non-Hermitian chiral-symmetric systems, *Phys. Rev. B* 100, 161105(R) (2019).
- [37] R. Kubo, M. Toda, N. Hashitsume, *Statistical Physics II*, in: Springer Series in Solid State Sciences, Springer Berlin, (1985).
- [38] J. H. Han, H. Lee, Spin chirality and Hall-like transport phenomena of spin excitations, *J. Phys. Soc. Jpn* 86 011007 (2017).
- [39] G. D. Mahan, *Many Particles Physics*, Plenum, New York, (1990).
- [40] Xiao-Gang Wen, *Quantum Field Theory of Many-Body Systems*, Oxford University Press, New York (2004).
- [41] K. Zyczkowski, P. Horodecki, A. Sanpera, M. Lewenstein, Volume of the set of separable states, *Phys. Rev. A* 58, 883 (1998).
- [42] D. J. Scalapino, S. R. White, S. C. Zhang, *Phys. Rev. Lett.* 68, 2830 (1992).
- [43] M. B. Plenio, Logarithmic Negativity: A Full Entanglement Monotone That is not Convex, *Phys. Rev. Lett.* 95, 090503 (2005).
- [44] G. Perez, W. Witczak-Krempa, Entanglement negativity between separated regions in quantum critical systems, *Phys. Rev. Res.* 6, 023125 (2024).
- [45] P. Calabrese, John Cardy, Quantum quenches in 1+1 dimensional conformal field theories, *J. Stat. Mech.* 064003 (2016).
- [46] D. Bianchini, O. A. Castro-Alvaredo, B. Doyon, E. Levi, F. Ravanini, *J. Phys. A: Math. Theor.* 48 04FT01 (2014).
- [47] P. Calabrese, Entanglement and thermodynamics in non-equilibrium isolated quantum systems, *Physica A* 504, (2018) 31.
- [48] Y. R. Kartik, R. R. Kumar, Scaling theory for non-Hermitian topological transitions, *J. Phys. Condens. Matter* 37, 125602 (2025).